



# Revealing the Nanoarchitectonics of Amyloid $\beta$ -Aggregation on Two-Dimensional Biomimetic Membranes by Surface-Enhanced Infrared Absorption Spectroscopy

Manyu Zhu,<sup>[a, b]</sup> Li Zeng,<sup>[c]</sup> Zihao Li,<sup>[a, b]</sup> Chen Wang,<sup>[a, b]</sup> Lie Wu,<sup>\*[a]</sup> and Xiue Jiang<sup>\*[a, b]</sup>

The in vivo folding of amyloid  $\beta$  ( $A\beta$ ) is influenced by many factors among which biomembrane interfaces play an important role. Here, using surface-enhanced infrared absorption (SEIRA) spectroscopy and atomic force microscopy (AFM), the adsorption, structure, and morphology of  $A\beta$ 42 aggregating on different two-dimensional interfaces were investigated. Results show that interfaces facilitate the aggregation of  $A\beta$ 42 and are conducive to the formation of homogeneous aggregates, while the aggregates vary on different interfaces. On hydrophobic interfaces, strong hydrophobic interactions with the C-terminus

of  $A\beta$ 42 result in the formation of small oligomers with a small proportion of the  $\beta$ -sheet structure. On hydrophilic interfaces, hydrogen-bonding interactions and electrostatic interactions promote the formation of large aggregate particles with  $\beta$ -sheet structure. The hydration repulsion plays an important role in the interaction of  $A\beta$ 42 with interfaces. These findings help to understand the nature of  $A\beta$ 42 adsorption and aggregation on the biomembrane interface and the origin of heterogeneity and polymorphism of  $A\beta$ 42 aggregates.

## Introduction

Alzheimer's disease (AD) is a type of neurodegenerative disease caused by the impaired function of neuronal cells that leads to cognitive decline and reduced social adaptation.<sup>[1–3]</sup> Clinically, amyloid plaques formed by  $\beta$ -amyloid ( $A\beta$ ) aggregation have been found outside the brain cells of AD patients. Therefore, it is widely believed that soluble aggregates or insoluble fibers from  $A\beta$  deposit on brain cells, which damage cell membrane permeability, further inducing oxidative stress and the resultant apoptosis is one of the pathogenesises of AD.<sup>[4–7]</sup> Generally,  $A\beta$  consists of 39–43 amino acids, among which  $A\beta$ 40 and  $A\beta$ 42 are the most abundant and also the main component of amyloid plaques in the brain of AD patients. Although the physiological concentration of  $A\beta$ 40 is about 10 times higher

than that of  $A\beta$ 42, the latter is more prone to aggregation and directly related to AD pathology.<sup>[8–12]</sup>  $A\beta$ 42 can be divided into three parts: the soluble N-terminal region composed of polar amino acids (1–15), the hydrophobic C-terminal region composed of amino acids (28–42) and the middle connection region (16–27). The disordered N-terminal is not involved in the aggregation of  $A\beta$ 42, and the C-terminal and middle regions are essential for the aggregation of intermediates.<sup>[13,14]</sup>

In recent years, more and more evidence suggests that the early soluble  $A\beta$  oligomer is the main species that causes the dysfunction and death of nerve cells.<sup>[10,15–19]</sup> In vivo studies have found that  $A\beta$  aggregates can form ion channels on biomembrane, destroying the permeability of cell membrane, and that the number of amyloid plaques is not directly related to the decline of cognitive function<sup>[20–23]</sup> and the removal of amyloid plaques does not interrupt the development of neurodegeneration.<sup>[24]</sup> It is not very clear how these ion channels are formed and what factors are affecting such processes, but both biomembranes and biomimetic membrane interfaces can promote the structural transformation of  $A\beta$  from random coil to  $\beta$ -sheet, and then the formation of mature aggregates.<sup>[25–29]</sup> Studying the kinetics, structural changes and driving forces during the interaction of  $A\beta$  on biomembrane interfaces is of significant importance for revealing the mechanism of the pathogenesis and progression of AD. However, the complexity and variability of biomembrane interfaces and the heterogeneity of  $A\beta$  aggregates bring great challenges to study the initial stage of  $A\beta$  aggregation on the interface. Therefore, it is particularly important to build a suitable biomimetic membrane interface model and capture the real-time information of  $A\beta$  aggregation to explore the aggregation process of  $A\beta$  on two-dimensional interfaces.

Self-assembled monolayers (SAMs) are good models to explore the adsorption process of peptides on the interface by

[a] M. Zhu, Z. Li, C. Wang, Dr. L. Wu, Prof. Dr. X. Jiang  
State Key Laboratory of Electroanalytical Chemistry  
Changchun Institute of Applied Chemistry, Chinese Academy of Sciences  
Changchun, Jilin 130022 (P. R. China)  
E-mail: lwu@ciac.ac.cn  
jiangxiue@ciac.ac.cn

[b] M. Zhu, Z. Li, C. Wang, Prof. Dr. X. Jiang  
School of Applied Chemistry and Engineering  
University of Science & Technology of China  
Hefei, Anhui 230026 (P. R. China)

[c] L. Zeng  
State Key Laboratory of Environmental Chemistry and Ecotoxicology  
Research Center for Eco-Environmental Sciences, Chinese Academy of Sciences  
Beijing, 100085 (P. R. China)

 Part of a joint Special Collection of ChemistryOpen, Analysis & Sensing and Chemistry-Methods focusing on "Biosensing and Imaging: Methods and Applications". Please visit the collection page to view all contributions.

 © 2023 The Authors. Published by Wiley-VCH GmbH. This is an open access article under the terms of the Creative Commons Attribution Non-Commercial License, which permits use, distribution and reproduction in any medium, provided the original work is properly cited and is not used for commercial purposes.

taking advantage of their controllable surface morphology and chemical functional groups which could modulate the adsorption behavior of biomolecules.<sup>[30–34]</sup> So far, molecular dynamics simulations,<sup>[35,36]</sup> atomic force microscopy,<sup>[37–39]</sup> and spectroscopy techniques<sup>[40–44]</sup> have been used to illustrate the folding dynamics and structural changes of A $\beta$  on different interfaces. Studies have shown that a two-dimensional interface can promote A $\beta$  aggregation and accelerate fiber formation.<sup>[30,31]</sup> On the hydrophobic surface of C18, A $\beta$ 40 and A $\beta$ 42 firstly nucleated, and then extended and aggregated in an exponential growth mode.<sup>[45]</sup> Moreover, molecular dynamics simulations suggest that the adsorption and further aggregation of A $\beta$  on different SAMs are a competitive process between A $\beta$ -SAM and water-SAM.<sup>[46]</sup> These findings provide important clues for studying the aggregation process of A $\beta$  at the interface, but the specific structural information about interface adsorbed A $\beta$  is mostly limited to molecular dynamics simulation results lacking supporting from experimental data. However, the specific structure of A $\beta$  at the interface is highly dynamic, and the lack of real-time in situ information limits the in-depth understanding of A $\beta$  aggregation. In this work, we investigated the dynamics, structure and morphology information of A $\beta$ 42 on SAMs with different terminal groups at an early stage by surface-enhanced infrared absorption (SEIRA) spectroscopy and atomic force microscopy (AFM) to reveal the nature of A $\beta$ 42 aggregation at the molecular level.

## Results and Discussion

### Characterization of self-assembled monolayers

Three thiol molecules with different terminal groups ( $-\text{CH}_3$ ,  $-\text{OH}$ ,  $-\text{COOH}$ ), namely dodecanethiol (DT), 11-mercaptoundecanol (MU) and 11-mercaptoundecanoic acid (MUA) were selected to assemble monolayers with different interfacial properties on a gold surface. The self-assembly process could be readily monitored in-situ by SEIRA spectroscopy (Figure 1a). With bare gold film immersed in a background solution (here, ethanol) as a reference, characteristic peaks (detailed assignments shown in Table 1) could be observed immediately after the addition of three thiol molecules with a final concentration of 1 mM. Asymmetric stretching ( $\nu_{\text{as}}$ ) and symmetric stretching ( $\nu_{\text{s}}$ ), and bending vibration ( $\delta$ ) of  $\text{CH}_2$  groups were observed for the three SAMs. The peak positions of  $\nu_{\text{as}}(\text{CH}_2)$  for the three SAMs are nearly identical and in a low wavenumber region. Since  $\nu_{\text{as}}(\text{CH}_2)$  is very sensitive to the conformation of the  $\text{CH}_2$  group, the lower wavenumber indicates a more well-ordered structure of the SAMs.<sup>[47]</sup> The same position of  $\nu_{\text{as}}(\text{CH}_2)$  suggests that well-ordered SAMs are formed and the packing order of alkyl chains are nearly the same for three SAMs due to the long alkyl chain (C10) in the three thiol molecules used. For DT SAM,  $\nu_{\text{as}}(\text{CH}_3)$ ,  $\nu_{\text{s}}(\text{CH}_3)$ , and  $\delta_{\text{as}}(\text{CH}_3)$  are observed at  $2960\text{ cm}^{-1}$ ,  $2875\text{ cm}^{-1}$ , and  $1380\text{ cm}^{-1}$ , respectively, which should be unique for DT molecule.<sup>[48]</sup> However,  $\nu_{\text{as}}(\text{CH}_3)$  and  $\nu_{\text{s}}(\text{CH}_3)$  were also observed for the MU and MUA SAMs (middle and lower panel of

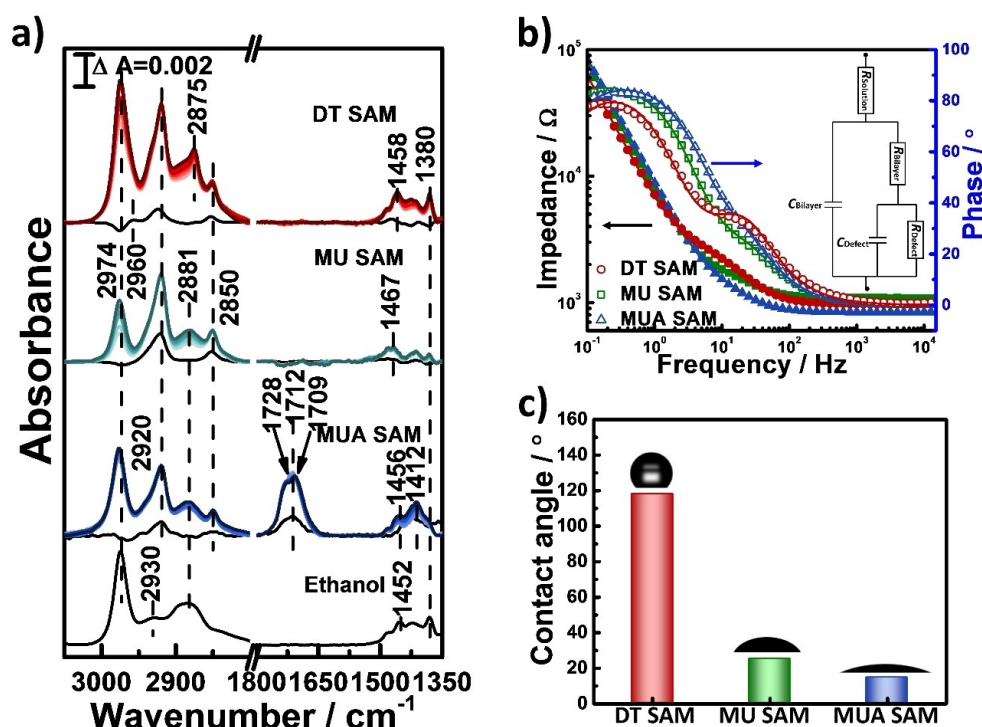


**Figure 1.** (a) In situ monitoring the formation of SAMs (from top to bottom: DT SAM, MU SAM, MUA SAM). The spectra were recorded at different time points (from bottom to top: 10 s, 30 s, 1 min, 5 min, 10 min, 12 min, 32 min, 65 min). The bottom panel shows the SEIRA spectrum of ethanol molecule. (b) The EIS spectra of DT (red circles), MU (green squares) and MUA (blue triangles) SAMs; filled and empty symbols refer to the phase angle and the magnitude of the impedance, respectively. Lines represent the result of fitting the equivalent circuit. Inset: Equivalent circuit used for fitting the data. (c) Water contact angle of DT, MU, MUA SAMs.

**Table 1.** Assignments of SEIRA spectral peaks for three SAMs and ethanol molecule.

Peak assignment	Wavenumber [cm <sup>-1</sup> ]			
	DT monolayer	MU monolayer	MUA monolayer	Ethanol molecule
$\nu_{as}(\text{CH}_3)$	2960	–	–	2974
$\nu_{as}(\text{CH}_2)$	2920	2920	2920	2930
$\nu_s(\text{CH}_3)$	2875	–	–	2881
$\nu_s(\text{CH}_2)$	2850	2850	2850	weak
$\nu(\text{C}=\text{O})$	–	–	1712	–
$\delta(\text{CH}_2)_n$	1458	1467	1456	1452
$\delta_{as}(\text{CH}_3)$	1380	–	–	1380

Figure 1a) which do not contain any CH<sub>3</sub>. This is caused by the interference from ethanol molecules that were used as background solution. As shown in the top panel of Figure 1a, at the initial stage of adsorption (black line, recorded 10 s after addition of DT), a negative peak at 2974 cm<sup>-1</sup> was observed, and positive peaks at 2960 cm<sup>-1</sup> and 2875 cm<sup>-1</sup> were also noted. Considering that ethanol may have pre-adsorbed on the gold film during the collecting of the background spectrum, the negative peak at 2974 cm<sup>-1</sup> was assigned to the  $\nu_{as}(\text{CH}_3)$  of ethanol molecules due to the replacement of interfacial ethanol by adsorbed DT molecules, just as the negative peak in  $\nu(\text{OH})$  region was found to be caused by the displacement of water molecules upon the adsorption of nanomaterials to the interface in H<sub>2</sub>O environment in our previously reported work.<sup>[49]</sup>

Thus, positive peaks at 2960 cm<sup>-1</sup> and 2875 cm<sup>-1</sup> were assigned to the  $\nu_{as}(\text{CH}_3)$  and  $\nu_s(\text{CH}_3)$  of DT molecules. The negative peak at 2974 cm<sup>-1</sup> changed to a positive one, and  $\nu_{as}(\text{CH}_3)$  of the DT molecule at 2960 cm<sup>-1</sup> overlapped with 2974 cm<sup>-1</sup> ( $\nu_{as}(\text{CH}_3)$  of ethanol molecules) with elapsed time possibly due to the recombination, reorientation and co-adsorption of ethanol molecules on the interface during the self-assembly process. It should be noted that the initial replacement of ethanol was also observed in the adsorption process of MU and MUA molecules, which suggests the ultra-sensitivity of SEIRA spectroscopy in interfacial analysis. For the MU SAM, characteristic absorption peaks of alkyl chains were observed. For the MUA SAM, a vibration peak at 1712 cm<sup>-1</sup> attributed to  $\nu(\text{C}=\text{O})$  in COOH was observed at initial adsorption, which is the characteristic vibration absorption peak of MUA.<sup>[50]</sup> Moreover, this  $\nu(\text{C}=\text{O})$  peak of COOH gradually split into two peaks centered at 1709 cm<sup>-1</sup> and 1728 cm<sup>-1</sup>, indicating different hydrogen bond environments of the COOH groups in the MUA SAM due to the deprotonation of COOH during the self-assembly process.<sup>[50]</sup> Thus, the splitting of carbonyl peak indicates the COOH groups of MUA form an intermolecular hydrogen bond network after SAM formation.

The formation of DT, MU, MUA SAMs was further confirmed by electrochemical impedance spectroscopy (EIS), as shown in Figure 1b. A modified Randles equivalent circuit (inset of Figure 1b) that has been proposed to model membranes supported on nanostructured Au film<sup>[51]</sup> was used to fit the impedance data. The experimental data are fitted well with the simulated curves, and the calculated capacitance values of DT, MU and MUA SAMs on gold nanofilms are 1.67  $\mu\text{F cm}^{-2}$ , 2.72  $\mu\text{F cm}^{-2}$  and 3.22  $\mu\text{F cm}^{-2}$  respectively, which are consistent

with reported values in the literature,<sup>[52]</sup> indicating the successful formation of SAMs. Since the alkyl chain orders of three SAMs are basically the same indicated by the nearly identical peak position of  $\nu_{as}(\text{CH}_2)$  (Figure 1a), the variation of the capacitance values may have been caused by the difference in terminal groups. This is also supported by the finding that the “small to large” variation trend of capacitance values of SAMs follows the increasing size of terminal groups of the three thiol molecules. This indicates the influence of the chemical nature of the terminal groups on the interfacial properties of SAMs. Furthermore, the contact angle of water droplets on the interface was used to characterize the hydrophilicity of the SAMs.<sup>[53]</sup> Water droplets will spread out on a hydrophilic interface while they will converge on hydrophobic interfaces. Thus, the more hydrophilic the interface is, the greater the wetting degree, and the smaller the contact angle. As shown in Figure 1c, the contact angles of water on the three SAMs are 118° for DT SAM, 24.9° for MU SAM, and 14.4° for MUA SAM, respectively. The terminal group of DT molecule is a methyl group (–CH<sub>3</sub>), which is hydrophobic and small, endowing DT SAM with great hydrophobicity. The MU molecule has a terminal hydroxyl group (–OH), which is hydrophilic and neutral, resulting in a moderate hydrophilic interface. MUA SAM is more hydrophilic than MU SAM due to its negative charges from its terminal carboxyl groups. All these results suggest that well-packed SAMs with different interfacial properties were successfully prepared.

### In situ SEIRA spectroscopic monitoring of the adsorption and aggregation of A $\beta$ 42 on SAMs

The adsorption and initial folding process of the A $\beta$ 42 monomer on SAMs with different interfacial properties were monitored in real time by in situ SEIRA spectroscopy (Figure 2). As shown in Figure 2a–c, characteristic peaks of protein (amide I and amide II) with growing intensity could be clearly observed within 8 h for three SAMs, indicating that A $\beta$ 42 monomer could adsorb on these two-dimensional interfaces. Amide I band is the combination of the C=O stretching vibration and the N–H bending vibration of the amide bond, and the C=O vibrations of each peptide bond in the protein couple with each other. Since the coupling pattern is determined by the secondary structure of the protein, the amide I band is widely used to analyze the secondary structure of proteins.<sup>[54]</sup> The variation of

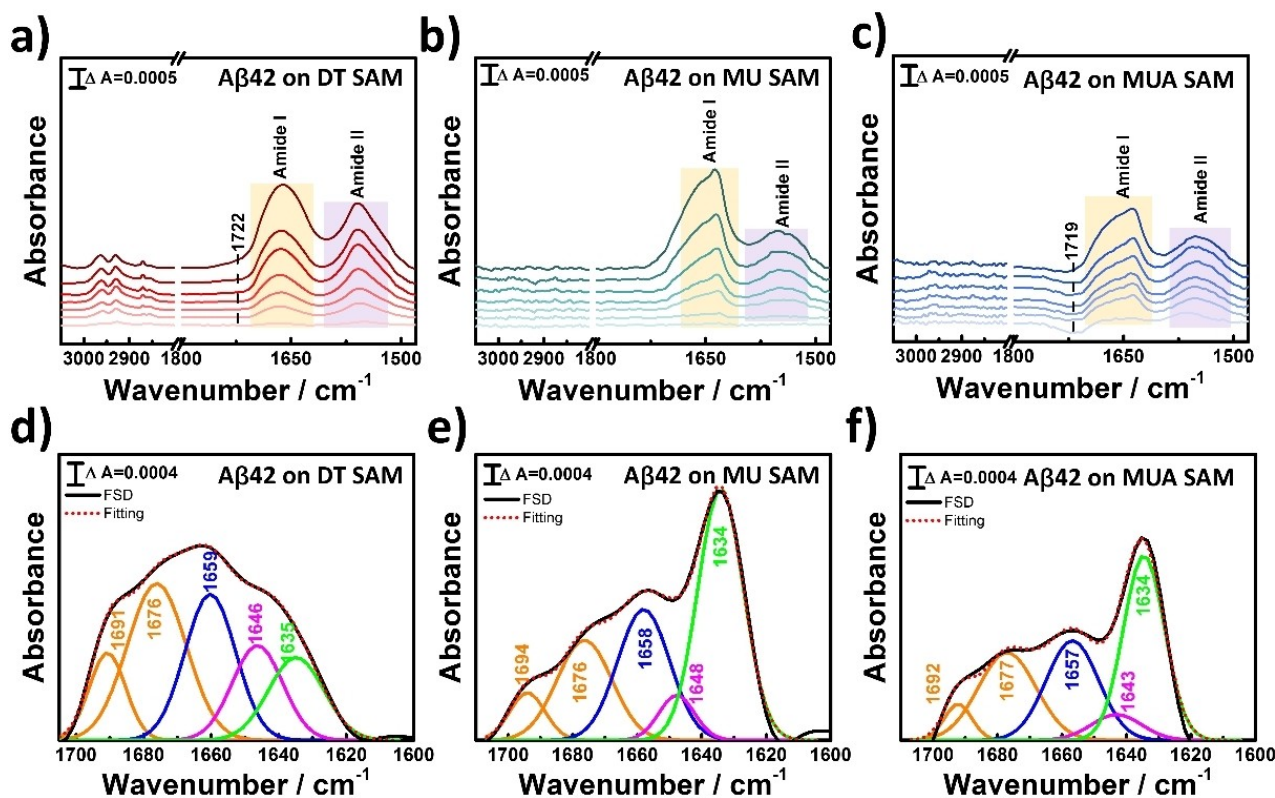


**Figure 2.** In situ monitoring of the adsorption and folding process of A $\beta$ 42 on DT (a), MU (b) and MUA (c) SAMs by SEIRAS. The spectra were recorded at different time points (from bottom to top: 1 min, 5 min, 10 min, 30 min, 1 h, 2 h, 8 h, respectively). Deconvoluted amide I band of the SEIRA spectra of A $\beta$ 42 on DT (d), MU (e) and MUA (f) SAMs at 8 h (the black solid lines and red dot lines represent FSD spectra and fitting curves respectively; the orange, blue, pink and green solid lines represent the  $\beta$ -turn,  $\alpha$ -helix, random coil and  $\beta$ -sheet secondary structures, respectively).

both peak position and shape suggests that the folding of the A $\beta$ 42 monomer on the three SAMs is different (Figure 2a–c). The structure of the A $\beta$ 42 monomer is rich in  $\alpha$ -helices and random coils, which were converted to  $\beta$ -sheet secondary structures in the A $\beta$  aggregates.<sup>[55,56]</sup>

To further reveal the secondary structures of A $\beta$  aggregates formed on three different SAMs, Fourier self-deconvolution (FSD) analysis<sup>[57]</sup> was performed to deconvolute the broad amide I bands. Spectra shown in Figure 2a–c were thus further deconvoluted to show sub bands corresponding to  $\alpha$ -helix,  $\beta$ -sheet,  $\beta$ -turn, and random coil secondary structures as shown in Figure 2d–f. The estimated contents of secondary structures are summarized in Table 2. On the DT SAM (shown in Figure 2d), the content of  $\alpha$ -helix/random coil of adsorbed A $\beta$  is estimated to about 42%, which is lower than for the A $\beta$ 42 monomer and close to the value for a A $\beta$ 42 oligomer on the lipid membrane surface reported by Mrdenovic et al.<sup>[58]</sup> This suggests that the A $\beta$ 42 monomer adsorbed on the hydrophobic DT SAM and

folded into an oligomer with very low content of  $\beta$ -sheet structures (15.6%). Meanwhile, a series of positive absorption peaks appeared in the CH<sub>n</sub> region from 2800 cm<sup>-1</sup> to 3000 cm<sup>-1</sup>, and a tiny peak at 1722 cm<sup>-1</sup> was noted. The former might originate from surface-adsorbed A $\beta$ 42 or conformational changes of the underlayer DT SAM. The latter is attributed to  $\nu$ (C=O) of A $\beta$ 42 side chain amino acids containing carboxyl groups, since the underlying DT molecule has no absorption in this region. Considering that amino acids containing carboxyl groups in the A $\beta$ 42 peptide chain, including Ser8, Tyr10, Gln15, Ser26 and Asn27, are all located at the polar N-terminus, it is speculated that the hydrophobic C-terminal region (29–42) of A $\beta$ 42 interacts with the DT SAM through hydrophobic interactions and folded into an  $\alpha$ -helix structure that was embedded in the alkyl chain region. The N-terminus (1–26) is exposed to the solvent. Therefore, the positive peaks located from 2800 cm<sup>-1</sup> to 3000 cm<sup>-1</sup> could be attributed to  $\nu$ (CH<sub>n</sub>) in the A $\beta$ 42 side chains and the conformational change of DT SAM was induced by the interaction with A $\beta$ 42. In contrast, no obvious change was observed in the CH<sub>n</sub> region for the MU and MUA SAMs (Figure 2b,c). This suggests that A $\beta$ 42 mainly interacts with MU and MUA SAMs at the hydrophilic interface without affecting the underlying alkyl chains, which is dramatically different from the findings for the DT SAM, indicating a different interaction mode.

**Table 2.** Contents of secondary structures of A $\beta$ 42 on different SAMs.

A $\beta$ 42 on different SAMs	Content of secondary structure			
	$\alpha$ -helix	Random coil	$\beta$ -sheet	$\beta$ -turn
A $\beta$ 42 on DT SAM	25.4%	16.4%	15.6%	42.6%
A $\beta$ 42 on MU SAM	25.1%	5.9%	42.5%	26.5%
A $\beta$ 42 on MUA SAM	25.8%	6.6%	38.2%	29.4%

For A $\beta$ 42 adsorbed on MU and MUA SAMs, the shapes of the amide I bands are quite similar (Figure 2e,f) and the variation of secondary structure content is within 4% (Table 2), which indicates that the A $\beta$ 42 aggregates formed on these two SAMs are of similar structure. However, the contents of  $\beta$ -sheet structure (42.5% on MU SAM and 38.2% on MUA SAM) are significantly higher than that on DT SAM (15.6%), as shown in Table 2. The  $\alpha$ -helix contents of the A $\beta$ 42 aggregates formed on the three SAMs are basically the same, while the random coil content significantly decreased from 16.4% for DT SAM to 5.9% for MUA SAM and 6.6% for MUA SAM. This indicates that the interaction with MU and MUA SAM induces more  $\beta$ -sheet structure formation, which is believed to be from the converting of random coil structure. These effects should originate from the different interaction modes between A $\beta$ 42 and these three SAMs.

A clearly negative peak of  $\nu(\text{C}=\text{O})$  was observed right after the addition of A $\beta$ 42 on the MUA SAM (Figure 2c), which suggests that the addition of A $\beta$ 42 might destroy the hydrogen bond network among the underlay MUA molecules and change the orientation of the C=O moiety in the COOH groups. Many studies have shown that A $\beta$ 42 can bind electrostatically to anionic phospholipids or anionic SAMs through positively charged amino acids such as Arg5 and Lys16,<sup>[59,60]</sup> and could form hydrogen bonding with OH group of sphingolipid polysaccharide molecules,<sup>[61]</sup> promoting A $\beta$ 42 adsorbing and folding. Thus, it is believed that A $\beta$ 42 adsorbed on the MUA SAM through electrostatic attraction and hydrogen bonding interaction, induced the spectral change of C=O in COOH groups. In contrast, hydrogen bonding interactions account for the interaction force between A $\beta$ 42 and MU SAM. Considering significantly more  $\beta$ -sheet structure is observed on both the MU and the MUA SAMs, it is reasonable to deduce that the hydrogen bonding interaction promotes the formation of  $\beta$ -sheet structures. It should be noted that the sub-band positions are slightly different for aggregates formed on MU and MUA SAM, indicating that the detailed intermolecular packing is different for A $\beta$ 42 adsorbed on these two SAMs (Figure 2e,f). Thus, it is deduced that the electrostatic attraction might only affect the intermolecular packing, possibly due to the facilitating effect on short-range hydrogen bonding interactions.<sup>[49,62]</sup> Besides, A $\beta$ 42 is a short peptide chain which only has three positively charged amino acids, two of which (Arg5 and Lys16) could participate in electrostatic attraction while the other one (Lys28) is believed to participate in an intermolecular salt bridge with Asp23.<sup>[63,64]</sup> Thus, the electrostatic attraction interaction between A $\beta$ 42 and MUA SAM is relatively weak. This might partially account for the non-obvious effect of electrostatic attraction interaction on the secondary structure of adsorbed A $\beta$ 42.

### Adsorption kinetics of A $\beta$ 42 on SAMs

The interfacial property significantly affects the secondary structure of adsorbed A $\beta$ 42. A $\beta$ 42 folded to a structure with little amount of  $\beta$ -sheets on the hydrophobic interface of the

DT SAM, while the more hydrophilic interfaces of the MU/MUA SAMs promote the formation of  $\beta$ -sheet structure. To better understand the effect of the interfacial property on the interaction between A $\beta$ 42 and SAMs, the adsorption kinetics of A $\beta$ 42 adsorption on three SAMs were analyzed (Figure 3).

The shape of the amide I band was greatly affected by the secondary structure of A $\beta$ 42 and closely relates to the adsorption orientation of the protein, while the influence of these two factors on the amide II band was much less pronounced.<sup>[48,54]</sup> Thus, the adsorption kinetics were analyzed through the time-dependent peak intensity of amide II band of A $\beta$ 42. As shown in Figure 3, the adsorption kinetic is the fastest and the adsorption quantity is the largest on the hydrophobic DT SAM. In contrast, for hydrophilic SAMs, the adsorption kinetic is slow and the adsorption quantity is small. Thus, although A $\beta$ 42 monomer is soluble in aqueous solution, hydrophobic interaction is the strongest and most effective interaction among the three interaction forces in the interaction with SAMs. It should be noted that the initial adsorption of A $\beta$ 42 on MUA SAM is faster than that on the MU SAM, which can also be seen in Figures 2b and 2c where the amide II peak could be clearly observed in the first spectrum recorded at 1 min for the MUA SAM. This is attributed to the long-range electrostatic interaction with MUA SAM, while on MU SAM short-range hydrogen-bonding interaction dominated.

In addition, long-range electrostatic interactions may facilitate the short-range hydrogen-bonding interaction on MUA SAM. The smaller adsorption quantity on the MUA SAM than on the MU SAM may be caused by the higher wetting degree observed for the MUA SAM (Figure 1c). We speculate that the hydration degree plays an important role in the adsorption of A $\beta$ 42 on interfaces. Due to its negative charge originating from the carboxylate terminal groups, the hydrogen-bonding networks of interfacial water on MUA SAM are stronger than those on MU SAM, and such a strong hydrogen-bonded hydrate layer at the interface increases the energy barrier of adsorption, which may lead to the smaller adsorption quantity. In contrast, on the hydrophobic DT SAM, where the interaction between

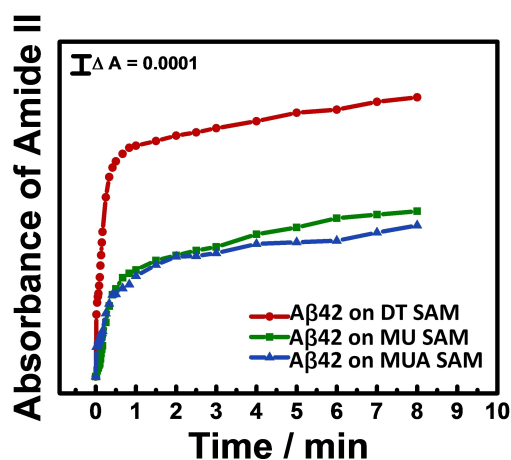


Figure 3. Adsorption kinetics derived from the time-dependent peak intensity of amide II band of A $\beta$ 42 on DT (red circles), MU (green squares) and MUA (blue triangles) SAMs.

water molecules and interface is quite weak, the hydration layer could be easily removed, resulting in a very small energy barrier of adsorption. Moreover, the C-terminus of A $\beta$ 42 is rich of hydrophobic amino acids.<sup>[13,14]</sup> The strong hydrophobic interaction and very weak energy barrier of dehydration result in the fastest adsorption kinetic and largest adsorption quantity on the hydrophobic DT SAM.

### AFM characterization of the morphology of A $\beta$ 42 aggregates on different SAMs

The adsorption process of A $\beta$ 42 on three SAMs was monitored by in-situ SEIRA spectroscopy, and the results showed that both the secondary structures of surface-adsorbed A $\beta$ 42 and the adsorption kinetics are different on the three different two-dimensional interfaces. Atomic force microscopy (AFM) was further used to obtain the morphology of A $\beta$ 42 aggregates that form on these interfaces and in bulk solution (Figures 4 and 6).

As shown in Figure 4, aggregates that form on the hydrophobic DT SAM are of small size, and no fiber-like morphology was observed (Figure 4a, d). This is consistent with the spectral data, which suggests that less  $\beta$ -sheet structure is formed. Considering the hydrophobic residues are located at the C-terminus, residues 29–42 could interact with the DT SAM through hydrophobic interactions (Figure 5a). Thus, the small aggregates on DT SAM may be small oligomers with an  $\alpha$ -helix at its C-terminus embedded in the SAM, which is the early stage of forming large aggregates and fiber-like morphology.<sup>[65,66]</sup> The aggregates formed on MU SAM not only contain larger particles

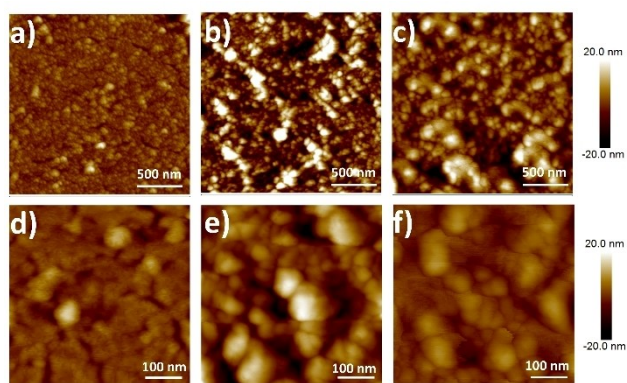


**Figure 4.** AFM images of DT (a, d), MU (b, e), MUA (c, f) SAMs after incubation in A $\beta$ 42 monomer solution for 8 h.

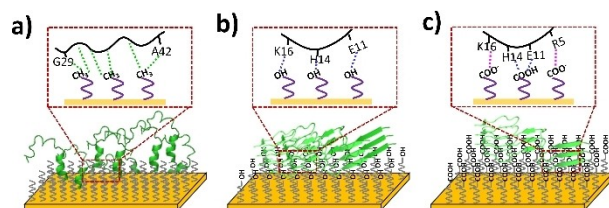


**Figure 5.** Surface aggregation models and possible mechanisms of A $\beta$ 42 on DT (a), MU (b) and MUA (c) SAMs.

(Figure 4b,e), but also appeared to be connected together to form initial fibers. It has been reported that Glu, His, and Lys can form hydrogen bonds with OH<sup>[59,67]</sup> and residues 1–9 have little connection with the  $\beta$ -hairpin motif during A $\beta$  aggregation.<sup>[68,69]</sup> Therefore, the possible mechanism of A $\beta$ 42 interacts with the MU SAM may operate through Lys16, His 14 and Glu11 (Figure 5b).

In contrast, on the MUA SAM, the aggregates are of similar lateral size of that on MU SAM, but no obvious connection between particles was observed (Figure 4c, f). These results are also in line with spectral data, which indicates that these large particles are of  $\beta$ -sheet structure, and might readily form initial fibers. As mentioned above, A $\beta$ 42 interacts electrostatically through Arg5 and Lys16 with MUA and forms hydrogen bonds through His14 and Glu11 (Figure 5c). The absence of a connection between particles on MUA SAM might be due to the large energy barrier of dehydration and relatively small adsorption quantity.

The morphology of A $\beta$ 42 aggregates that formed in bulk solution without the presence of two-dimensional interface was shown in Figure 6. The aggregates observed could be mainly categorized into two types: one is a typical amyloid fiber and the other is characterized as large aggregated amorphous particles.

At 0 h, no aggregate was observed, indicating that A $\beta$ 42 exists as monomer in solution. This also suggests that the adsorption of A $\beta$ 42 on different interfaces starts from monomers. After incubating for 12 h, even though some amyloid fibers with diameters of about 2 nm were observed, most of the A $\beta$ 42 still existed in monomeric form.<sup>[70]</sup> At 24 h of incubation, the probability of observation of amyloid fiber increases, and fibrous aggregates could always be observed in the field of view when scanning in different regions. Furthermore, large amorphous aggregates began to appear. With longer incubation times, the percentage of amyloid fiber increases. Thus, the two-dimensional interface can not only accelerate the aggregation of A $\beta$ 42, but also modulate the size and type of A $\beta$ 42 aggregates by controlling the interface properties. However, the variety of phospholipids and polysaccharides endows biomembranes with various dynamic interfacial properties,

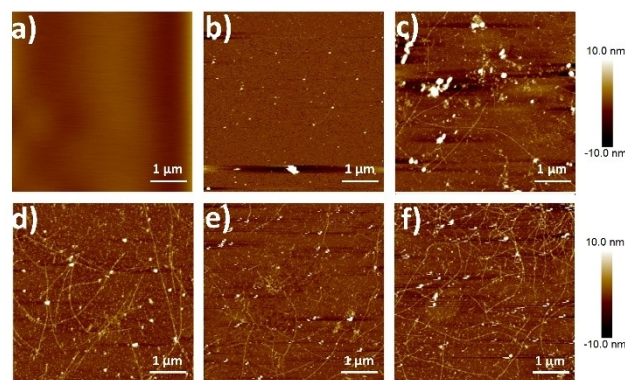


**Figure 6.** AFM images A $\beta$ 42 monomer solution incubated for 0 h (a), 12 h (b), 24 h (c), 36 h (d), 48 h (e) and 60 h (f).

which may imply that A $\beta$ 42 has great heterogeneity and polymorphism in the interaction and aggregation on biomembranes.

## Conclusion

In this work, we preliminarily explored the structure, kinetics, and morphologies of A $\beta$ 42 adsorbed on two-dimensional interfaces using self-assembled monolayers (SAMs) with different terminal groups as models. We found that the two-dimensional interface can significantly accelerate the aggregation of A $\beta$ 42, which is mainly due to the interaction between the two-dimensional interface and the A $\beta$ 42 monomer. The properties of the two-dimensional interface significantly affect the secondary structure and morphology of A $\beta$ 42 aggregates. On a hydrophobic interface, A $\beta$ 42 adsorbs on interface by hydrophobic interaction with the C-terminus, and mainly forms small oligomers with  $\alpha$ -helix structure which could penetrate into the alkyl chain region. In contrast, hydrophilic interfaces promote the formation of large aggregate particles with  $\beta$ -sheet structures through hydrogen-bonding interactions. Importantly, interfacial hydration plays an important role in the interaction between A $\beta$ 42 and the interface. The adsorption and aggregation of A $\beta$ 42 at interfaces is a complex process resulting from the balance of various interaction forces including hydrophobic, hydrogen-bonding and electrostatic interactions as well as dehydration of the interface. The synergistic or competitive interactions between these different forces in the biological environment of organisms may be the source of the aggregation heterogeneity and polymorphism of A $\beta$ 42 on biomembranes.

## Experimental Section

### Preparation of A $\beta$ 42 solution

For preparing the A $\beta$ 42 stock solution, A $\beta$ 42 powder (Sigma-Aldrich) was dissolved in hexafluoroisopropanol (HFIP). After sonication for 30 min, the solution was centrifuged at 12000 rpm for 10 min to remove potentially undissolved substances. The obtained clear solution was repackaged, and stored at  $-20^{\circ}\text{C}$ . For preparing the A $\beta$ 42 solution, HFIP was first dried with high-purity  $\text{N}_2$ , and 50  $\mu\text{L}$  NaOH (5 mM) were added and sonicated for 30 s. Freshly prepared A $\beta$ 42 solution was used for each experiment.

### SEIRA spectroscopy setup

SEIRA spectroscopy in the attenuated total reflection mode was used in this study. The spectroscopy setup has been described elsewhere.<sup>[49]</sup> Briefly, a silicon prism serving as internal reflection element was carefully polished with 1.0  $\mu\text{m}$  alumina powder until a fresh hydrophobic surface was exposed. After thoroughly washed with ultrapure water, the prism was immersed in 40% ammonium fluoride for 90 s to terminate the surface with hydrogen. The treated Si prism was heated to  $65^{\circ}\text{C}$  in a water bath, and 1:1:1 mixed solution of 0.03 M  $\text{NaAuCl}_4$ , 0.3 M  $\text{Na}_2\text{SO}_3$  + 0.1 M  $\text{Na}_2\text{S}_2\text{O}_3$  + 0.1 M  $\text{NH}_4\text{Cl}$ , and 2.5 vol% HF were injected onto the clean surface of the Si prism. The reaction was terminated by thoroughly rinsing

the surface with ultrapure water once a bright yellow gold film was formed (typically 90 s). Potential contaminants on the gold film were removed by electrochemical cycling in 0.1 M  $\text{H}_2\text{SO}_4$  until the cyclic voltammogram of polycrystalline gold appeared. As-prepared gold-coated prism was mounted into a home-built polytrifluoro-chloroethylene cell. SEIRA spectroscopy was performed in a Kretschmann-ATR configuration under an incident angle of  $60^{\circ}$  with a home-made accessory. All spectra were recorded in a spectral window of 4000 to  $800\text{ cm}^{-1}$  with a resolution of  $4\text{ cm}^{-1}$  using a vacuum FTIR spectrometer (VERTEX 80 V, Bruker, Ettlingen, Germany) with a liquid nitrogen-cooled MCT detector. Typically, 512 scans were accumulated for each spectrum.

**Formation and characterization of self-assembled monolayer (SAM)** Ethanol was added to the test cell where freshly prepared gold film was installed, and then gold film immersed in ethanol was recorded as background spectrum. Dodecanethiol (DT), 11-mercaptoundecanol (MU) and 11-mercaptoundecanoic acid (MUA) ethanol solution was added to reach a final concentration of 1 mM, and series sample spectra were recorded. After self-assembly for 65 min, the modified gold surface was thoroughly washed with ethanol and dried under high-purity  $\text{N}_2$ . The obtained SAMs were further characterized by electrochemical impedance spectroscopy (EIS) and contact angle measurement. EIS were recorded by PGSTAT302 N workstation equipped with FRA32 M module using three-electrode configuration: the modified SEIRA Au film, a Pt-plate, and a Ag/AgCl (3 M KCl) electrode serving as working, counter, and reference electrodes, respectively. Spectra were monitored in a frequency range of 0.1 to 100 kHz at open circuit potential and an amplitude of 5 mV (rms value) in 10 mM PB electrolyte. For contact angle measurement, 1  $\text{cm} \times 1\text{ cm}$  Si wafer was used and the gold film and SAMs were prepared with the same procedure described above. Contact angle of SAMs were obtained by contact angle goniometer (Ramehart 200) by sessile drop method. A water droplet of 5–7  $\mu\text{L}$  was deposited on SAMs and the contact angle was measured within five seconds.

### In situ SEIRA spectroscopy monitor the adsorption and aggregation of A $\beta$ 42 on SAMs

After the formation of SAMs, 450  $\mu\text{L}$  10 mM PB (pH 7.0) was added and then equilibrated with background solution for certain time. Before sample spectra were acquired, a reference spectrum of the background solution was recorded. Concomitant with the addition of A $\beta$ 42 in 50  $\mu\text{L}$  5 mM NaOH (reaching a final concentration of 25  $\mu\text{M}$ ), a series of spectra were recorded. The amide I bands were resolved by Fourier self-deconvolution (FSD) technique through OPUS software, which used a Lorentz line with a full width of  $25\text{ cm}^{-1}$  at half-height and a resolution enhancement factor of 2.<sup>[71]</sup> The peak position was fixed during curve fitting, and the peak intensity and width were adjusted to minimize the root mean square between the experimental spectrum and the fitting curve.

### Morphology characterization of A $\beta$ 42

Morphology of A $\beta$ 42 adsorbed on different SAMs: Vacuum-evaporated gold film on mica was used as substrate for morphology characterization, and modified with DT, MU and MUA under the same procedure as SEIRA spectroscopy. After incubation with 25  $\mu\text{M}$  A $\beta$ 42 for 8 h, the substrate was thoroughly washed with 10 mM PB and ultra-pure water. Then, the substrates were dried at room temperature. Morphology of A $\beta$ 42 that incubated in solution: 25  $\mu\text{M}$  A $\beta$ 42 in 10 mM PB (pH 7.0) was incubated at  $37^{\circ}\text{C}$  to induced aggregation. 10  $\mu\text{L}$  of incubated solution was sampled and dropped on the freshly cleaved mica surface every 12 h. After incubating for 3 min, the PB solution was washed off with ultra-

pure water and dried at room temperature. Morphology of A $\beta$ 42 was obtained by atomic force microscope (AFM) imaging in tapping mode with PPP-NCHR (Nanosensor) tips.

## Acknowledgements

This work was financially supported by The Inter-Government International Science and Technology Innovation Cooperation project from Ministry of Science and Technology of China (2022YFE0113000), the National Science Fund for Distinguished Young Scholars (22025406), the National Natural Science Foundation of China (22074138), Science and Technology Innovation Foundation of Jilin Province (YDZJ202101ZYTS039, 20220101065JC), and the Youth Innovation Promotion Association of CAS (Grant No. 2020233).

## Conflict of Interest

The authors declare no conflict of interest.

## Data Availability Statement

The data that support the findings of this study are available from the corresponding author upon reasonable request.

**Keywords:** aggregates · amyloid- $\beta$  protein · atomic force microscopy · surface-enhanced infrared absorption spectroscopy · two-dimensional interface

- [1] S. Gandy, *J. Clin. Invest.* **2005**, *115*, 1121–1129.
- [2] J. A. Hardy, G. A. Higgins, *Science* **1992**, *256*, 184–185.
- [3] A. D. Korczyn, *Alzheimer's Dementia* **2008**, *4*, 176–178.
- [4] J. Hardy, D. J. Selkoe, *Science* **2002**, *297*, 353–356.
- [5] H. W. Querfurth, F. M. LaFerla, *New Engl. J. Med.* **2010**, *362*, 329–344.
- [6] A. Martel, L. Antony, Y. Gerelli, L. Porcar, A. Fluit, K. Hoffmann, I. Kiesel, M. Vivaudou, G. Fragneto, J. J. de Pablo, *J. Am. Chem. Soc.* **2017**, *139*, 137–148.
- [7] B. R. Sahoo, S. J. Cox, A. Ramamoorthy, *Chem. Commun.* **2020**, *56*, 4627–4639.
- [8] M. Serra-Batiste, M. Ninot-Pedrosa, M. Bayoumi, M. Gairi, G. Maglia, N. Carulla, *Proc. Natl. Acad. Sci. USA* **2016**, *113*, 10866–10871.
- [9] S. L. Bernstein, N. F. Dupuis, N. D. Lazo, T. Wyttenbach, M. M. Condrón, G. Bitan, D. B. Teplow, J.-E. Shea, B. T. Ruotolo, C. V. Robinson, M. T. Bowers, *Nat. Chem.* **2009**, *1*, 326–331.
- [10] N. J. Economou, M. J. Giammona, T. D. Do, X. Zheng, D. B. Teplow, S. K. Buratto, M. T. Bowers, *J. Am. Chem. Soc.* **2016**, *138*, 1772–1775.
- [11] W. Zheng, M. Y. Tsai, P. G. Wolynes, *J. Am. Chem. Soc.* **2017**, *139*, 16666–16676.
- [12] G. Bitan, M. D. Kirkitadze, A. Lomakin, S. S. Vollers, G. B. Benedek, D. B. Teplow, *Proc. Natl. Acad. Sci. USA* **2003**, *100*, 330–335.
- [13] P. C. Ke, M.-A. Sani, F. Ding, A. Kakinien, I. Javed, F. Separovic, T. P. Davis, R. Mezzenga, *Chem. Soc. Rev.* **2017**, *46*, 6492–6531.
- [14] K. S. Li, D. L. Rempel, M. L. Gross, *J. Am. Chem. Soc.* **2016**, *138*, 12090–12098.
- [15] I. Benilova, E. Karran, B. De Strooper, *Nat. Neurosci.* **2012**, *15*, 349–357.
- [16] J. C. Stroud, C. Liu, P. K. Teng, D. Eisenberg, *Proc. Natl. Acad. Sci. USA* **2012**, *109*, 7717–7722.
- [17] N. Gao, Z. Liu, H. Zhang, C. Liu, D. Yu, J. Ren, X. Qu, *Angew. Chem. Int. Ed.* **2022**, *61*, e202115336.
- [18] H. Zhang, C. Hao, A. Qu, M. Sun, L. Xu, C. Xu, H. Kuang, *Angew. Chem. Int. Ed.* **2020**, *59*, 7131–7138; *Angew. Chem.* **2020**, *132*, 7197–7204.
- [19] H. Geng, D. Gao, Z. Wang, X. Liu, Z. Cao, C. Xing, *Chin. J. Chem.* **2022**, *40*, 524–538.
- [20] C. G. Glabe, *Neurobiol. Aging* **2006**, *27*, 570–575.
- [21] J. Zhang, J. Tan, R. Pei, S. Ye, *Langmuir* **2020**, *36*, 1530–1537.
- [22] X. Wang, C. Wang, H. Chu, H. Qin, D. Wang, F. Xu, X. Ai, C. Quan, G. Li, G. Qing, *Chem. Sci.* **2020**, *11*, 7369–7378.
- [23] M. Tian, L. Shen, *ACS Macro Lett.* **2020**, *9*, 813–818.
- [24] C. Holmes, D. Boche, D. Wilkinson, G. Yadegarfar, V. Hopkins, A. Bayer, R. W. Jones, R. Bullock, S. Love, J. W. Neal, E. Zotova, J. A. R. Nicoll, *Lancet* **2008**, *372*, 216–223.
- [25] I. W. Hamley, *Nat. Chem.* **2010**, *2*, 707–708.
- [26] P. N. Nirmalraj, J. List, S. Battacharya, G. Howe, L. Xu, D. Thompson, M. Mayer, *Sci. Adv.* **2020**, *6*, eaaz6014.
- [27] S. M. Butterfield, H. A. Lashuel, *Angew. Chem. Int. Ed.* **2010**, *49*, 5628–5654; *Angew. Chem.* **2010**, *122*, 5760–5788.
- [28] V. Lattanzi, I. André, U. Gasser, M. Dubackic, U. Olsson, S. Linse, *Proc. Natl. Acad. Sci. USA* **2021**, *118*, e2112783118.
- [29] J. Zhou, L. Venturelli, L. Keiser, S. K. Sekatskii, F. Gallaire, S. Kasas, G. Longo, T. P. J. Knowles, F. S. Ruggeri, G. Dietler, *ACS Nano* **2021**, *15*, 944–953.
- [30] Q. Wang, N. Shah, J. Zhao, C. Wang, C. Zhao, L. Liu, L. Li, F. Zhou, J. Zheng, *Phys. Chem. Chem. Phys.* **2011**, *13*, 15200–15210.
- [31] T. Ragaliauskas, M. Mickevicius, R. Budvytyte, G. Niaura, B. Carbonnier, G. Valincius, *J. Colloid Interface Sci.* **2014**, *425*, 159–167.
- [32] M. J. McMasters, R. P. Hammer, R. L. McCarley, *Langmuir* **2005**, *21*, 4464–4470.
- [33] M. R. Zimmermann, S. C. Bera, G. Meisl, S. Dasadhikari, S. Ghosh, S. Linse, K. Garai, T. P. J. Knowles, *J. Am. Chem. Soc.* **2021**, *143*, 16621–16629.
- [34] V. Dubois, D. Serrano, X. Zhang, S. Seeger, *Anal. Chem.* **2020**, *92*, 4963–4970.
- [35] Q. Wang, C. Zhao, J. Zhao, J. Wang, J.-C. Yang, X. Yu, J. Zhen, *Langmuir* **2010**, *26*, 3308–3316.
- [36] D. Q. Huy Pham, P. Krupa, H. L. Nguyen, G. La Penna, M. S. Li, *J. Phys. Chem. B* **2020**, *124*, 3300–3314.
- [37] M. Ewald, S. Henry, E. Lambert, C. Feuillie, C. Bobo, C. Cullin, S. Lecomte, M. Molinari, *Nanoscale* **2019**, *11*, 7229–7238.
- [38] W. Lee, S. W. Lee, G. Lee, D. S. Yoon, *J. Alzheimer's Dis. Rep.* **2018**, *2*, 41–49.
- [39] J. Liu, M. Tian, L. Shen, *Chem. Commun.* **2020**, *56*, 3147–3150.
- [40] M. Calero, M. Gasset, *Methods Mol. Biol.* **2005**, *299*, 129–151.
- [41] F. Vosough, A. Barth, *ACS Chem. Neurosci.* **2021**, *12*, 473–488.
- [42] J. Wang, T. Yamamoto, J. Bai, S. J. Cox, K. J. Korshavn, M. Monette, A. Ramamoorthy, *Chem. Commun.* **2018**, *54*, 2000–2003.
- [43] C. R. Fields, S. S. Dicke, M. K. Petti, M. T. Zanni, J. P. Lomont, *J. Phys. Chem. Lett.* **2020**, *11*, 6382–6388.
- [44] J. Han, J. Yoon, J. Shin, E. Nam, T. Qian, Y. Li, K. Park, S.-H. Lee, M. H. Lim, *Nat. Chem.* **2022**, *14*, 1021–1030.
- [45] J. Zhai, T. H. Lee, D. H. Small, M. I. Aguilar, *Biochemistry* **2012**, *51*, 1070–1078.
- [46] J. Zhao, Q. Wang, G. Liang, J. Zheng, *Langmuir* **2011**, *27*, 14876–14887.
- [47] M. D. Porter, T. B. Bright, D. L. Allara, C. E. D. Chidsey, *J. Am. Chem. Soc.* **1987**, *109*, 3559–3568.
- [48] L. Zeng, L. Wu, L. Liu, X. Jiang, *Anal. Chem.* **2016**, *88*, 11727–11733.
- [49] L. Wu, L. Zeng, X. Jiang, *J. Am. Chem. Soc.* **2015**, *137*, 10052–10055.
- [50] X. Jiang, K. Ataka, J. Heberle, *J. Phys. Chem. C* **2008**, *112*, 813–819.
- [51] M. Stelzle, G. Weissmuller, E. Sackmann, *J. Phys. Chem.* **1993**, *97*, 2974–2981.
- [52] P. Ramirez, R. Andreu, A. Cuesta, C. J. Calzado, J. J. Calvente, *Anal. Chem.* **2007**, *79*, 6473–6479.
- [53] M. Kind, C. Woell, *Prog. Surf. Sci.* **2009**, *84*, 230–278.
- [54] P. Roach, D. Farrar, C. C. Perry, *J. Am. Chem. Soc.* **2005**, *127*, 8168–8173.
- [55] P. C. Ke, R. Zhou, L. C. Serpell, R. Riek, T. P. J. Knowles, H. A. Lashuel, E. Gazit, I. W. Hamley, T. P. Davis, M. Fandrich, D. E. Otzen, M. R. Chapman, C. M. Dobson, D. S. Eisenberg, R. Mezzenga, *Chem. Soc. Rev.* **2020**, *49*, 5473–5509.
- [56] N. Benseny-Cases, M. Cocera, J. Cladera, *Biochem. Biophys. Res. Commun.* **2007**, *361*, 916–921.
- [57] F. Cao, L. Wang, X. Jiang, L. Guo, *RSC Adv.* **2013**, *3*, 17214–17221.
- [58] D. Mrdenovic, Z. Su, W. Kutner, J. Lipkowski, P. Pieta, *Nanoscale Adv.* **2020**, *2*, 3467–3480.
- [59] K. Ikeda, K. Matsuzaki, *Biochem. Biophys. Res. Commun.* **2008**, *370*, 525–529.

- [60] G. Gao, M. Zhang, P. Lu, G. Guo, D. Wang, T. Sun, *Angew. Chem. Int. Ed.* **2015**, *54*, 2245–2250; *Angew. Chem.* **2015**, *127*, 2273–2278.
- [61] K. Matsuzaki, *Acc. Chem. Res.* **2014**, *47*, 2397–2404.
- [62] L. Wu, X. Jiang, *Langmuir* **2020**, *36*, 1094–1102.
- [63] A. T. Petkova, R. D. Leapman, Z. H. Guo, W. M. Yau, M. P. Mattson, R. Tycko, *Science* **2005**, *307*, 262–265.
- [64] J. Khandogin, C. L. Brooks, *Proc. Natl. Acad. Sci. USA* **2007**, *104*, 16880–16885.
- [65] R. Qi, Y. Luo, B. Ma, R. Nussinov, G. Wei, *Biomacromolecules* **2014**, *15*, 122–131.
- [66] Y. Sun, A. Kaminen, Y. Xing, P. Faridi, A. Nandakumar, A. W. Purcell, T. P. Davis, P. C. Ke, F. Ding, *Small* **2019**, *15*, 1805166.
- [67] K. Mori, M. I. Mahmood, S. Neyra, K. Matsuzaki, T. Hoshino, *J. Phys. Chem. B* **2012**, *116*, 5111–5121.
- [68] A. T. Petkova, W. M. Yau, R. Tycko, *Biochemistry* **2006**, *45*, 498–512.
- [69] T. Takeda, D. K. Klimov, *J. Phys. Chem. B* **2009**, *113*, 11848–11857.
- [70] T. Hu, S. Wang, C. Chen, J. Sun, X. Yang, *Anal. Chem.* **2017**, *89*, 2606–2612.
- [71] P. M. Bummer, *Int. J. Pharmaceut.* **1996**, *132*, 143–151.

---

Manuscript received: November 29, 2022

Revised manuscript received: January 13, 2023